Fluorescent Probes

Design and Development of Axially Chiral Bis(naphthofuran) Luminogens as Fluorescent Probes for Cell Imaging

Valmik P. Jejurkar,[a] Gauravi Yashwantrao,[a] Pawan Kumar,[b] Suditi Neekhra,[c] Parimal J. Maliekal,[d] Purav Badani,[d] Rohit Srivastava,[c] and Satyajit Saha*[a]

Abstract: Designing chiral AIEgens without aggregation-induced emission (AIE)-active molecules externally tagged to the chiral scaffold remains a long-standing challenge for the scientific community. The inherent aggregation-caused quenching phenomenon associated with the axially chiral (*R*)-[1,1′-binaphthalene]-2,2′-diol ((*R*)-BINOL) scaffold, together with its marginal Stokes shift, limits its application as a chiral AIE-active material. Here, in our effort to design chiral luminogens, we have developed a design strategy in which 2-substituted furans, when appropriately fused with the BINOL scaffold, will generate solid-state emissive materials with high thermal and photostability as well as colour-tunable properties. The excellent biocompatibility, together with the high fluorescence quantum yield and large Stokes shift, of one of the luminogens stimulated us to investigate its cell-imaging potential. The luminogen was observed to be well internalised and uniformly dispersed within the cytoplasm of MDA-MB-231 cancer cells, showing high fluorescence intensity.

Introduction

The breakthrough in the discovery of luminescent materials has unleashed a number of opportunities for research and development in the area of light-emitting devices.[1,2] Understanding the concept of luminescence has allowed the scientific community to control the light-emitting properties of molecules as well as propound innovative solutions in the field of optical materials.[3–7] However, although fluorescent materials have diverse applications in areas ranging from optoelectronic devices and sensors to biological sciences, they often experience the iniquitous aggregation-caused quenching (ACQ) effect.[8,9] These molecules, although highly fluorescent in the solution state, become non-emissive in concentrated or aggregated states, thereby limiting their applications. However, with the advent of the phenomenon known as aggregation-induced emission (AIE), the research on AIE luminogens (AIEgens) has reached celestial heights.

AIEgens are mostly characterised by rotor-like structures, and the constrained motion of the rotors has been identified as one of the major causes of AIE. However, aggregation alone does not trigger fluorescence. The highly viscous microenvironment as well as non-covalent supramolecular interactions also contribute to trigger strong fluorescent emission.[10,11] The AIE phenomenon has enhanced the number of organic fluorophores, and significant endeavour has been made in the pursuit of novel AIEgens for optoelectronic materials.[12–16]

Among the plethora of AIEgens that have been developed, chiral AIEgens specifically have received tremendous attention owing to their ability to enantiodiscriminate chiral analytes.[17–28] AIE fluorophores are normally accessed by two well-recognised approaches, either by structurally tuning the existing AIEgens or by appending AIEgenic molecules to ACQ luminophores. Analogously, chiral AIEgens have also been successfully synthesised by fusing well-known achiral AIEgens to chiral scaffolds such as sugars, amino acids or axially chiral [1,1′-binaphthalene]-2,2′-diol (BINOL; Figure 1).[17–28] Nevertheless, design strategies that employ amino acids and sugars lead to AIEgens with poor thermal stability that lack scope for wavelength tunability. BINOL, vastly explored in asymmetric catalysis[29–33] and bearing a tremendous resemblance to the rotor-like structures of typical AIEgens such as tetraphenylethene (TPE) or tetraphenylsiloles, has been used to design chiral luminogens through the appendage of well-known AIEgens at appropriate positions of BINOL (Figure 1).[34–36] However, these existing design strategies are mostly limited to scaffolds such as TPE or tetraphenylsiloles. The dearth of protocols to generate

[a] V. P. Jejurkar, G. Yashwantrao, Dr. S. Saha
Department of Speciality Chemicals Technology
Institute of Chemical Technology (ICT)
Mumbai 400019 (India)
E-mail: ss.saha@ictmumbai.edu.in
[b] P. Kumar
Department of Biotechnology, BIT Mesra
Ranchi (India)
[c] S. Neekhra, Prof. R. Srivastava
Department of Biosciences and Bioengineering
IIT Bombay
Bombay (India)
[d] P. J. Maliekal, Dr. P. Badani
Department of Chemistry
University of Mumbai
Mumbai (India)
Supporting information and the ORCID identification number(s) for the author(s) of this article can be found under:
https://doi.org/10.1002/chem.202004942.

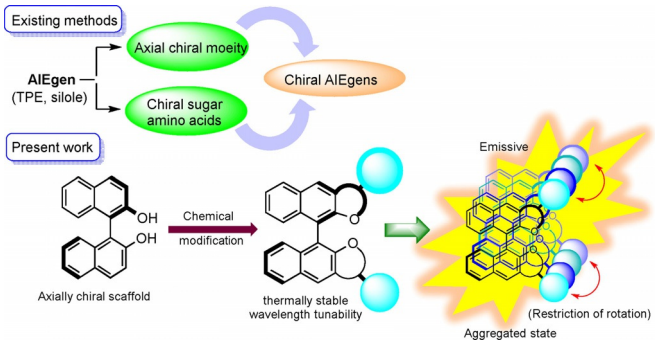

Figure 1. Rational design of chiral AIEgens.

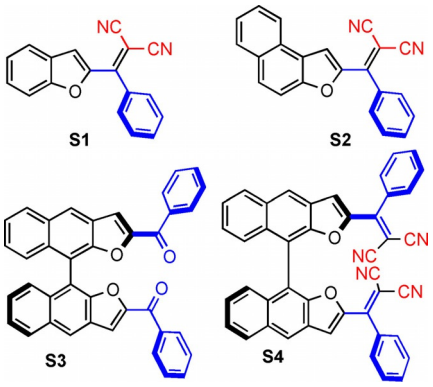

Figure 2. Structures of the designed AIEgens **S1**–**S4**.

chiral AIEgens without any AIEgens (e.g., TPE or tetraphenylsilole) externally tagged to the chiral scaffold remains a long-standing challenge. Therefore, modifying (*R*)-BINOL to design an AIE probe without any externally appended luminogenic material would be highly desirable to provide an alternative strategy for the development of chiral AIE materials possessing high thermal stability as well as colour tunability for diverse applications. Yet, the molecular design of chiral AIEgens based on the above-mentioned concept is highly challenging because of the inherent ACQ phenomenon associated with the (*R*)-BINOL scaffold, which makes them unsuitable for use as efficient AIEgens and hence limits their applications.

In our effort to design luminogens, we envisioned straightforward design criteria that accentuate the constrained rotation of the freely rotatable groups in the molecule through augmented intermolecular interactions as well as the disruption of molecular stacking in the solid state.[37] With this perspective, we considered furans that are non-emissive but if appropriately fused to the BINOL scaffold will generate chiral AIEgens with extended conjugation. The inbuilt molecular distortion due to the axial chirality of (*R*)-BINOL and the presence of electron-deficient phenacyl derivatives (-COPh/CPhC$(CN)_2$) attached to the furyl ring are likely to disrupt the π–π interactions and restrict internal rotations in the aggregated state accompanied by interrupted twisted intramolecular charge transfer (TICT). The inherent molecular distortion will purposefully restrict molecular stacking by the large-space hindering group, thereby endowing the fluorophores with enhanced emissive properties in the aggregated state (Figure 1).

Based on this rationale, in this study we have designed and synthesised four molecules (**S1**–**S4**; Figure) to evaluate the influence of benzo- and naphthofuran rings possessing electron-withdrawing phenacyl derivatives (-COPh/CPhC$(CN)_2$) as well as the influence of fusing the furan ring to the axially chiral (*R*)-BINOL on AIE in the aggregated state (Figure 1).

Compounds **S1** and **S2** were model compounds designed to compare the AIEgenic properties of achiral (**S1** and **S2**) and chiral luminogens (**S3** and **S4**). The initial goal of our research was to fuse the furan unit to phenol and naphthol rings to obtain **S1** and **S2**, respectively, and to derivatise the naphthol core of (*R*)-BINOL with furan to generate **S3** and **S4**. The straightforward base-catalysed cyclocondensation of the appropriate phenol derivatives with 2-bromoacetophenone was the key step to access all four fluorophores in reasonably good yields from commercially available starting materials. This easy synthetic protocol not only allowed access to novel chiral AIE-active molecules, but also established a new direction in the design of next-generation chiral luminogens with easy synthetic accessibility, high thermal stability and scope for wavelength tunability.

Thus, the crystallographic packing of luminogens **S1**–**S4**, supported by DFT calculations, their photophysical, electrochemical, thermal and AIE properties, together with their electronic circular dichroism (CD) spectra, are presented herein. The results demonstrate that the above strategy offers an effective approach to the design of solid-state luminescent materials with a remarkable AIE effect and significantly large Stokes shift.

Among the several established methods to acquire chiral information, circular dichroism (CD) is one of the most commonly used techniques and relies on the ground-state electronic conjugation of the chiral molecule. The CD spectra confirmed the transmission of the absolute stereochemistry of (*R*)-BINOL to both **S3** and **S4**, thereby converting them into chiral luminogens. However, chirality variation in the aggregated state often results in the obliteration of circular dichroism, and has frequently been observed in BINOL derivatives, which impedes their application in the condensed state.[38] Interestingly, straightforward functional group transformation to incorporate the dicyanovinylidene group resulted in the reversal of the CD behaviour of **S4** in the aggregated state as compared with **S3**.

Although the axially chiral BINOL has been successfully employed as a scaffold to build several fluorescent probes, poor water solubility and intrinsic π–π-stacking interactions along with the appearance of an emission band in the UV region due to a small Stokes shift have strictly limited their application as bioprobes due to strong biological autofluorescence interference.[39] However, the unique AIE properties exhibited by **S4**, which possesses a high fluorescence quantum yield (Φ_{agg} = 4.34%) and large Stokes shift (180 nm), coupled with excellent photo- and thermal stability as well as biocompatibility, prompted us to explore the potential of **S4** as a fluorescent bioprobe for cell imaging.

Imaging studies revealed that **S4** was well internalised within MDA-MB-231 cancer cells and uniformly dispersed in

the cytoplasm, showing high fluorescence intensity. Therefore, the above rational design of fusing non-luminescent furans onto an aromatic core could be a big boon for the development of AIE-active luminogens in the future.

Results and Discussion

Synthesis and characterisation

The AIEgens **S1**–**S4**, shown in Figure 2, were readily synthesised in good yields following the methodology highlighted in Scheme 1. The key steps were the base-catalysed substitution reaction, followed by cyclocondensation to fuse the 2-phenacylfuran component onto the benzene or naphthalene ring to construct benzo- and naphthofuran skeletons, respectively.

Thus, **S1** and **S2** were synthesised by treating 2-bromoacetophenone (**2**) with salicylaldehyde (**1 a**) or 2-hydroxynaphthaldehyde (**1 b**), respectively, by base-catalysed substitution, followed by cyclocondensation to generate the corresponding phenacyl derivatives **3** and **4**. Subsequent pyridine-mediated Knoevenagel condensation of **3** and **4** with malononitrile furnished **S1** and **S2**, respectively. Similarly, **S3** and **S4** were synthesised by the methylation of (*R*)-BINOL followed by formylation with *n*BuLi/*N*,*N*-dimethylformamide (DMF) to generate (*R*)-2,2′-dimethoxy-[1,1′-binaphthalene]-3,3′-dicarbaldehyde (**7**). Subsequent demethylation with BBr_3 in dichloromethane (DCM) generated (*R*)-2,2′-dihydroxy-[1,1′-binaphthalene]-3,3′-dicarbaldehyde (**8**). Base-catalysed substitution of **8** with 2-bromoacetophenone (**2**), followed by cyclocondensation furnished **S3**. Subsequent Knoevenagel condensation of **S3** by heating with malononitrile in pyridine at reflux afforded **S4**.

All the molecules were characterised by ^{1}H and ^{13}C NMR, IR, and mass spectrometric techniques. The synthetic procedures and spectral characterisation data of the luminogens **S1**–**S4** are provided in the Experimental Section as well as in the Supporting Information.

X-ray crystallographic analysis

To gain insights into the three-dimensional orientation of the molecules and their crystal packing, interplanar distances and torsion angles, we successfully grew single crystals of **S1**–**S3** by slow evaporation from $CHCl_3$.

The fluorophores **S1** and **S2** crystallised in the monoclinic system and **S3** in the triclinic system with space groups *P*21/*c*, *P*21/*n* and P21, respectively. The X-ray crystal structures of **S1**–**S3** are presented in Figure 3.

The single-crystal structures of both **S1** and **S2** present a twisted orientation. The phenyl ring has a non-coplanar orientation with respect to both the benzofuran and naphthofuran ring systems, making a dihedral angle of 52.95 and 52.26°, respectively. Images of the crystal packing in both **S1** and **S2** are shown in Figures S13–S16 in the Supporting Information. In **S1**, the molecules are partially stacked with two phenyl rings of neighbouring $CPhC(CN)_2$ groups facing each other with an interplanar distance of 3.472 Å between two molecules. The distinct deformation from planarity in the molecule is due to the installation of the bulky electron-deficient -COPh group, as manifested in the X-ray crystal structure, resulting in the mini-

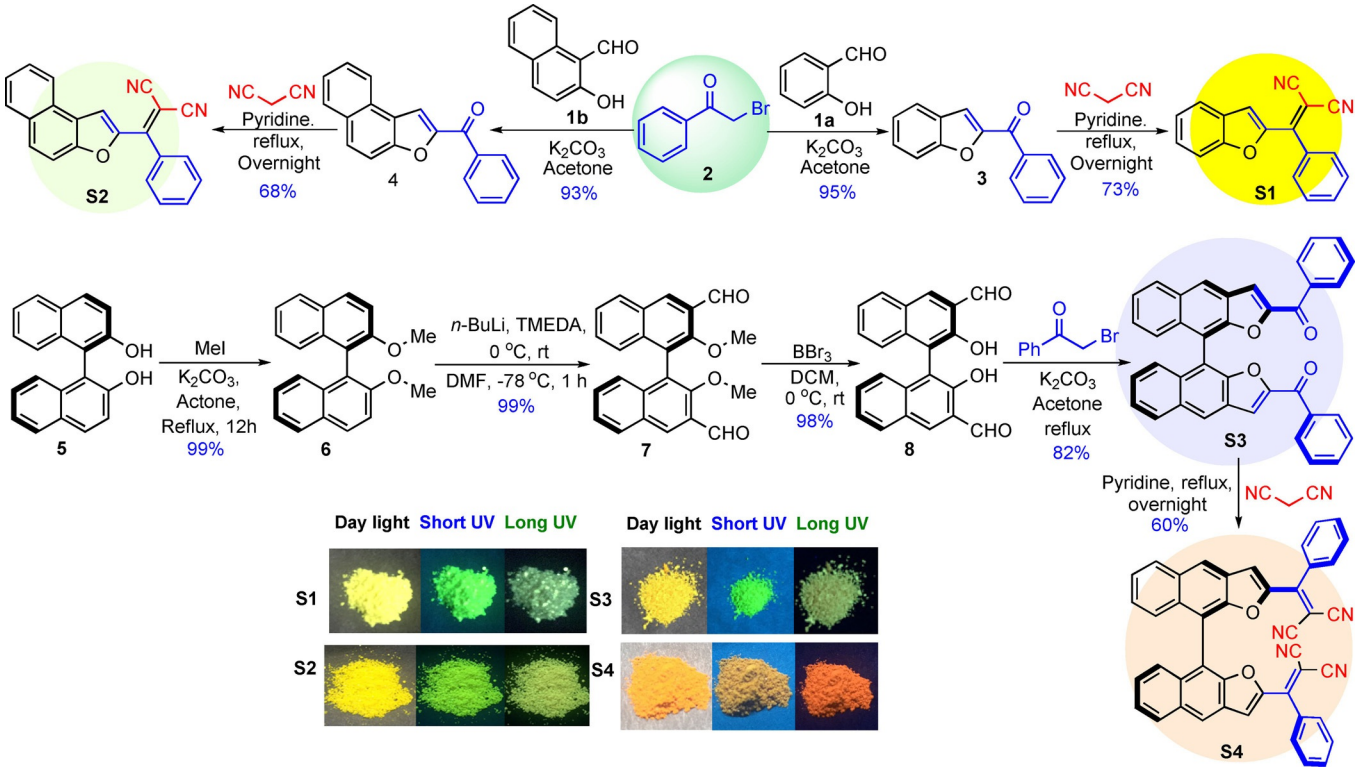

Scheme 1. Synthesis of AIEgens **S1**–**S4** and the appearance of the powdered forms of **S1**–**S4** in daylight and under short-UV (254 nm) and long-UV (365 nm) irradiation.

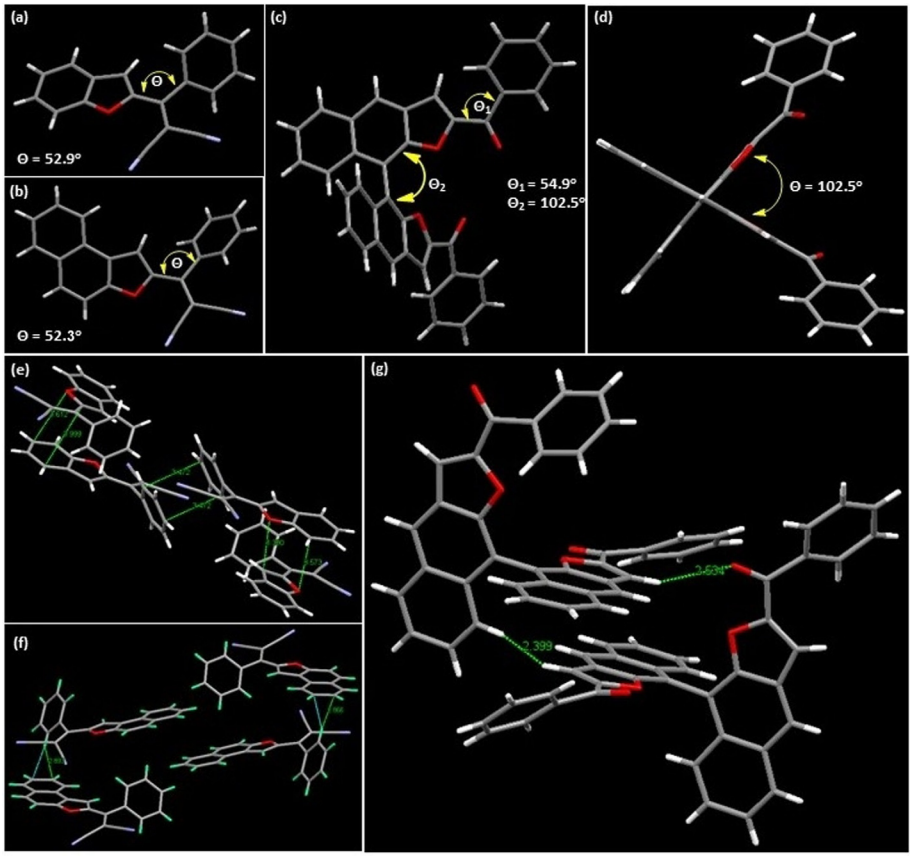

Figure 3. Single-crystal X-ray crystallographic representation of (a) **S1**, (b) **S2** and (c,d) **S3**, and the crystal packing of (e) **S1**, (f) **S2** and (g) **S3**, all identified by XRD analysis.

misation of π–π stacking. A similar arrangement was observed in the crystal packing of **S2**. The dihedral angle between the phenyl ring and the naphthofuran ring is 52.26°, which accounts for the non-existence of intermolecular stacking interactions within the crystal lattice. The naphthofuran moiety of **S2** is oriented in such a way that the molecules barely overlap each other in the crystal packing, resulting in a linear distance between the two molecules in the range 2.83–3.73 Å.

The crystal packing of **S3** also confirms the absence of any intermolecular π–π-stacking interactions, which is a consequence of the twisted conformation of **S3**, originating from the steric hindrance offered by the strong electron-withdrawing phenacyl group as well as the axial chirality of the (*R*)-BINOL scaffold with a dihedral angle of 102.5° between the two naphthofuran moieties, which form a scissor-like geometry. The bulky aromatic groups successfully instigate a twist in the molecular conformation, resulting in a torsion angle of 54.9° between the central BINOL plane and the -COPh group. As observed in Figure 3g, the naphthofuran rings are nearly orthogonal to each other, which impedes close π–π-stacking interactions between neighbouring molecules. Multiple short contacts, observed within the crystal lattice, are also beneficial for rigidifying the network and restricting intramolecular rotation, thereby greatly restraining non-radiative pathways and thus avoiding the quenching of fluorescence in the solid or aggregated state. The interplanar distances within the crystal lattice of **S3** are 3.534 and 2.399 Å, which suggests disruption of π–π-stacking interactions, resulting in the enhancement of emission intensity in the aggregated state.

Photophysical, electrochemical and thermal properties

The photophysical properties of the molecules **S1**–**S4** were evaluated by preparing a uniform 1 μM solution of each of the fluorophores in acetone. The UV/Vis spectra depicted in Figure 4 reveal that the absorption maxima of the compounds **S1**–**S4** range from 337 to 416 nm and can be attributed to π–π* electronic transitions. Compared with **S1**, the absorption maximum of **S2** is bathochromically shifted, which suggests strong intramolecular charge transfer within the molecule because of the extension of the fused ring system by one phenyl ring, resulting in a larger π-conjugated system than in **S1**.[40,41] A similar redshifted absorption maximum was also observed for **S4** as compared with **S3**.

The photoluminescence (PL) spectra of compounds **S1**--**S4** in acetone solution are also presented in Figure 4. The spectra exhibit emission maxima ranging from 410 to 561 nm, with significantly high Stokes shifts of 152 and 180 nm for **S3** and **S4**, respectively, which can be attributed to intramolecular charge transfer due to the donor–acceptor nature of the molecules, as is evidenced from the calculated HOMO–LUMO energy gaps (see Figure 7). It can also be noted that insertion

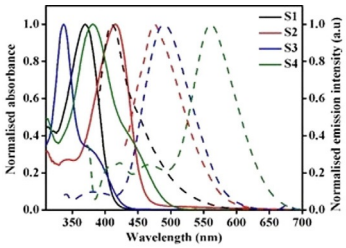

Compound	λ_{abs} [a] (nm)	λ_{em} [b] (nm)	Stokes shift nm	Stokes shift cm^{-1}
S1	370	410	40	2636
S2	416	475.5	59.5	3008
S3	337	489.5	152.5	9245
S4	381	561	180	8421

Figure 4. Normalised absorption (solid lines) and emission spectra (dotted lines) of the fluorophores **S1**–**S4** and the corresponding absorption and emission wavelengths and Stokes shifts. [a] λ_{abs} = absorption maxima wavelengths. [b] λ_{em} = emission maxima wavelengths. The scan step width used for PL measurement was 0.5 nm.

of the powerful electron-accepting -$C(CN)_2$ group into **S4** resulted in a bathochromically shifted emission spectrum compared with **S3**, effectively shifting the bluish-green emission of **S3** to the reddish-orange emission of **S4** in the solid state, thereby generating colour-tunable AIEgens.

Although **S2** and **S4** have a similar structural framework, the chirality enforced in the latter molecule leads to an apparent difference in their emission intensity as well as their Stokes shift.

The thermal stabilities of the fluorophores **S1–S4** were assessed by thermogravimetric analysis (TGA) and differential scanning calorimetry (DSC). Excitingly, very high thermal stabilities were observed for compounds **S3** and **S4** compared with **S1** and **S2** (Figure 5), which is a result of the structurally robust (*R*)-BINOL skeleton.

The thermal degradation temperature (T_d) indicates less than 2 and 8% degradation for **S3** and **S4** with 75 and 43% weight loss observed at around 475 and 446 °C, respectively. Although **S3** exhibited melting temperatures (T_m) of 265.89 and 464.70 °C in the first heating scan, no endo- or exothermic reactions were observed for **S4**, which implies exceptional thermal stability of the molecule with apparently no glass transition, crystallisation or melting taking place.

Solvatochromic properties of S1–S4

The high Stokes shifts of the fluorophores prompted us to investigate the effect of solvent polarity on the emission maxima of compounds **S1**–**S4**. The PL spectra of compounds **S1–S4** were recorded in solvents with graded polarity (toluene, THF, acetone, DMSO and DMF; see Figures S1 and S2 in the Supporting Information). The results revealed a normal positive solvatochromic effect for **S1**, **S3** and **S4** (see Table S1). Thus, in polar solvents, the formation of TICT states is favourable for these compounds, and increasing the solvent polarity promotes the intramolecular charge-transfer (ICT) character of the excited states of **S1**, **S3** and **S4**. However, the bathochromic shift of the absorption maximum displayed by **S2** in non-polar solvent can be attributed to probe–probe interactions. The extended conjugation and skew arrangement of the aromatic systems seem to be influenced by the peri hydrogen atoms of the naphthalene ring, causing such abnormal behaviour.[42]

Cyclic voltammetry and DFT calculations

Cyclic voltammetry and DFT calculations were performed to evaluate the electrochemical properties of the fluorophores **S1**–**S4** and the parameters obtained are presented in Figures 6 and 7, respectively. The redox potentials of **S1**, **S2**, **S3** and **S4**, which correspond to their HOMO energy levels, were determined to be −6.45, −6.39, −6.30 and −6.42 eV versus the normal hydrogen electrode (NHE), respectively, and the corresponding HOMO–LUMO bandgaps are 3.36, 2.99, 3.68 and 3.26 eV, respectively (Figure 6).

To better comprehend the electronic transitions as well as to evaluate the theoretical bandgaps of the fluorophores **S1--S4**, DFT calculations were performed at the DFT/B3LYP level of theory using the Gaussian 09 suite of programs.[43] Energy minimisation of the structures was carried out by using the 6-31 G basis set. Finally, the single-point energies of these optimised structures were calculated by using the 6-311G+(d,p) basis set. Also, the effect of solvent was accounted for by using a conductor-like polarisable continuum model implicit solvent, in this case dichloromethane. The cartesian coordinates along with the optimised energy-minimised structures of **S1**–**S4** are provided in Figure 7.

The DFT calculations revealed that for the fluorophores **S1** and **S2**, the electron distribution in the HOMO is centred on the benzo- and naphthofuran rings. For **S1**, the electrons are delocalised throughout the molecule in the LUMO. However, in

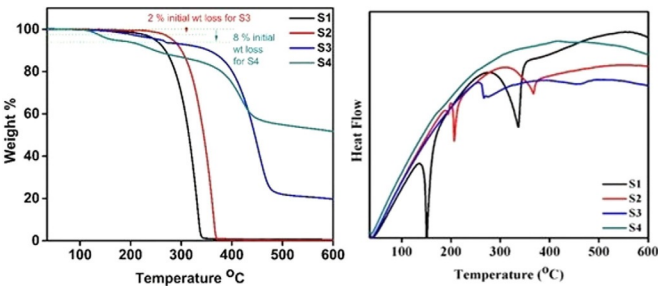

Figure 5. TGA-DSC thermograms of **S1–S4**.

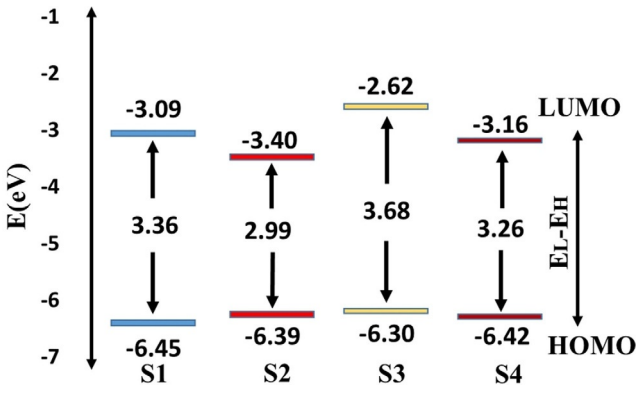

Figure 6. HOMO–LUMO energy gaps of **S1**–**S4** calculated experimentally from cyclic voltammetry data.

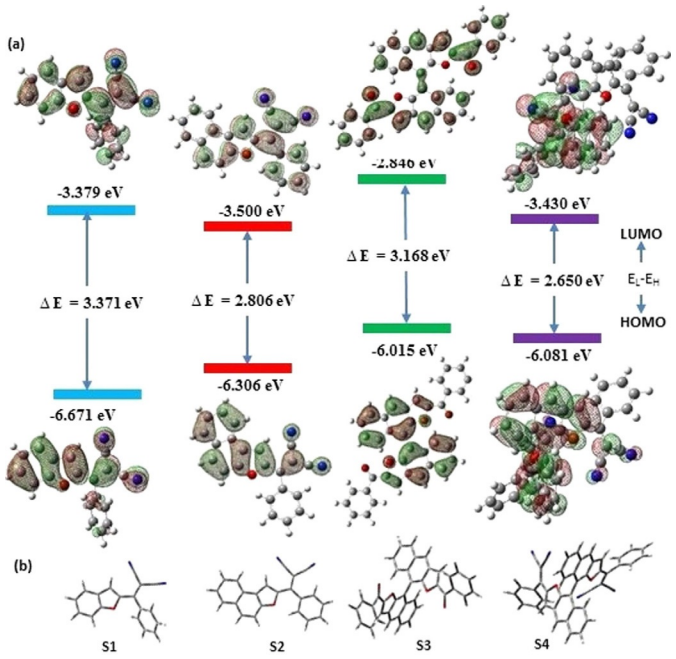

Figure 7. (a) Frontier molecular orbital diagrams of **S1**–**S4**. The energy levels were calculated in the gas phase by using DFT. The isosurface values of **S1**--**S4** are 0.022 a.u. (b) Energy-minimised structures of **S1**--**S4**.

Table 1. Theoretically and experimentally calculated HOMO–LUMO energy gaps of **S1**–**S4**.

Compd	Theoretical			Experimental
	E_{HOMO} [a.u.] [eV]	E_{LUMO} [a.u.] [eV]	E_{HL} [a.u.] [eV]	E_{HL} [eV]
S1	−0.246	−0.124	0.122	3.36
	−6.671	−3.379	(3.371)	
S2	−0.231	−0.128	0.103	2.99
	−6.306	−3.500	(2.806)	
S3	−0.221	−0.104	0.117	3.68
	−6.015	−2.846	(3.168)	
S4	−0.223	−0.126	0.097	3.26
	−6.081	−3.430	(2.650)	

the LUMO of **S2**, the electrons have shifted from the naphthyl ring towards the benzofuran ring and -CPhC(CN)$_2$. The distribution of electrons in the HOMO is quite similar for both **S3** and **S4** and is localised on the BINOL moiety. However, the electrons are distributed quite differently in the LUMOs of **S3** and **S4**. The electrons are homogeneously distributed over the entire skeleton in the LUMO of **S3**, whereas in the LUMO of **S4**, the electrons are localised on one ring system of (*R*)-BINOL. This undoubtedly suggests electron transfer within **S1**–**S4**. As predicted by the DFT calculations, the bandgaps for **S1** and **S2** are 3.371 and 2.806 eV, whereas those for **S3** and **S4** are 3.168 and 2.650 eV, respectively (Table 1). The decrease in the bandgap as we move from **S3** to **S4** is possibly due to the presence of the electron-withdrawing cyanovinylidene group, which is in accord with the experimentally derived results. A similar reduction in both the theoretically as well as experimentally calculated bandgaps is also evident as we move from **S1** to **S2**, which is possibly due to greater electron delocalisation within the naphthalene ring. The significant shift of the electron cloud upon excitation indicates the occurrence of TICT in the AIEgens, resulting in a larger Stokes shift. However, there is a slight discrepancy between the calculated and experimentally observed bandgaps, which is probably due to the DFT calculations being performed in the gas phase.[44]

Aggregation-induced emission properties of S1–S4

The intense emission enhancement observed in thin films of the molecules encouraged us to explore their PL properties in the aggregated state. Thus, the AIE features of the fluorescence probes **S1**–**S4** were investigated in acetone/water mixtures with different water contents (0–90%), and the recorded PL spectra are displayed in Figure 8.[45]

AIEgen **S1** displayed mild photoluminescence in pure acetone, which could be because of the non-irradiative decay pathway through a strong intramolecular charge-transfer process as a result of the uninterrupted rotation of the phenyl rings of the -CPhC(CN)$_2$ group. However, sharp enhancement of the photoluminescence intensity was observed when the water fraction (f_w) was increased from 10 to 40%. The enhancement in emission intensity is possibly due to the increased solvent polarity. Because the fluorophore possesses a larger dipole moment in the excited state (μ_E) than in the ground state (μ_G), on excitation, the solvent dipoles have a chance to reorient or relax around μ_E, which lowers the excited-state energy. As the solvent polarity gradually increased, the effect became more prominent, resulting in emission at longer wavelengths.[46]

However, beyond 40% H_2O, a sharp decrease in the luminescence intensity was observed, which can be accounted for by an intense ICT process. Careful evaluation of the X-ray crystal structure revealed that although there is an inherent twist in the molecule, the facially stacked phenyl rings separated by an interplanar distance of 3.42 Å could be the reason for the possible ACQ effect.

However, **S2** represents a perfect example of an aggregation-induced emissive luminogen, with the emission intensity gradually intensifying with increasing fraction of water, becoming a maximum at $f_w = 90\%$ H_2O. The difference in luminescence behaviour between **S1** and **S2** could be surmised by assessing the crystal structures of **S1** and **S2** represented in Figure 3. The analysis revealed that the naphthyl group is beneficial for avoiding intermolecular stacking. Additionally, multiple short intermolecular interactions were found throughout the crystal structure of **S2**, which could help rigidify the molecular conformation, thereby restraining the non-radiative pathways and enhancing the emission in the aggregated state. Furthermore, upon severe aggregation, the rotational motions of the phenyl rotors are also restricted, enhancing even further the induced luminescence in the aggregated state.

In the case of fluorophore **S3**, the luminescence intensity increased until 20% H_2O and then decreased until 50% H_2O.

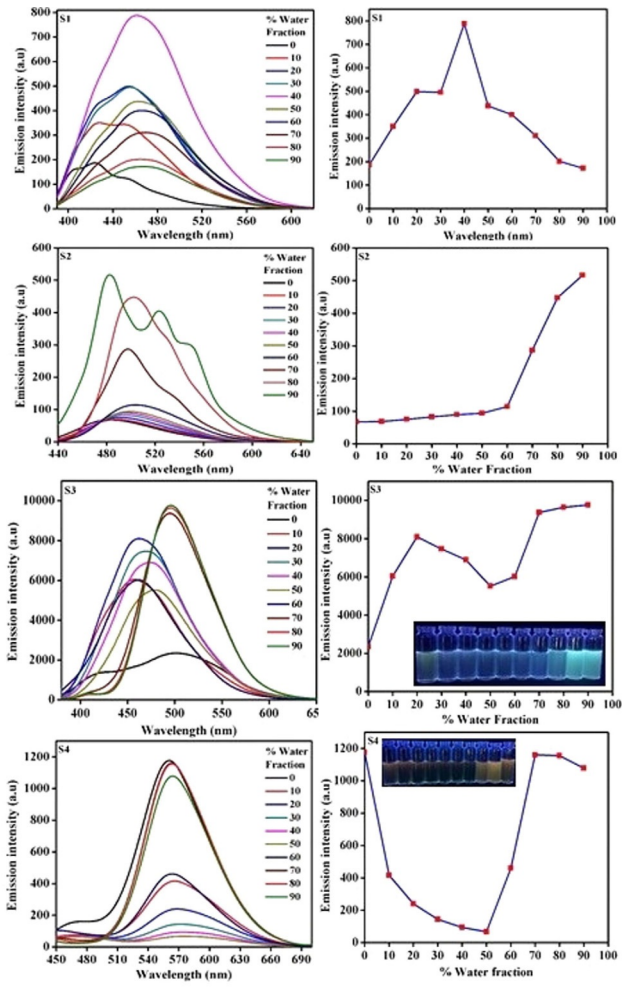

Figure 8. AIE behaviour of the luminogens **S1**–**S4** as evidenced by their PL spectra (excitation wavelength = 370, 416, 337, 381 nm for **S1**–**S4**, respectively; concentration = 1 μM in a mixture of acetone and 0–99% water) and plots of emission intensity as a function of water content in the solvent. The inserts display the PL of the highest and lowest aggregated states of **S3** and **S4**.

TICT through a non-radiative decay pathway is probably the reason for the gradual quenching of the emission intensity upon increasing the solvent polarity, and for the bathochromically shifted emission peak. The solvatochromic phenomenon demonstrated here can be attributed to the donor–acceptor (D–A) nature of the luminogen **S3**. The addition of water beyond $f_w = 70\%$ reduced the solvating power of the aqueous mixture to such an extent that luminogen S3 was unable to dissolve, thereby initiating the process of aggregate formation.

The nanoaggregates possess an interior polarity higher than the external surface polarity.[37,47] Therefore, the aggregates are transformed into an aggregation-induced locally excited state with a strained structure that is slightly destabilised energetically due to the low environmental polarity. This destabilisation results in the widening of the HOMO–LUMO energy gap, which causes the blueshifted emission (479 to 461 nm) observed for **S3**. Moreover, severe aggregation resulted in restricted intramolecular rotation of the phenyl ring and suppressed the TICT-inducing enhanced emission in the aggregated state. Further addition of water resulted in stronger emission until f_w reached 90%. A 4.2-fold enhancement in the emission intensity was observed for the highest aggregated state of **S3** at 90% H_2O compared with the pure acetone solution of **S3**.

For luminogen **S4**, initially, a very high photoluminescence intensity was observed, which then showed a dramatic drop in the luminescence intensity followed by a gradual decrease until f_w equalled 50% H_2O. The decrease in the emission intensity with a concomitant bathochromic shift of the emission peaks on increasing the solvent polarity could be because of the initiation of the ICT process, resulting in the quenching of the emission intensity through a non-radiative decay pathway. The addition of water beyond $f_w = 50\%$ resulted in the rapid enhancement of the photoluminescence intensity until reaching a maximum at $f_w = 70\%$, beyond which there was a slight drop in the emission intensity until $f_w = 90\%$ H_2O. The higher solvent polarity resulted in the formation of the aggregated state, which does not allow free rotation of the rotors, resulting in the enhanced emission intensity. Interestingly, no change in the emission wavelength was observed beyond $f_w = 50\%$ H_2O.

A comparison of the AIE behaviour of **S1**--**S4** revealed that the minor structural variations in **S1**--**S4** could explain the differences in the AIE trends.

Abnormal AIE behaviour was observed for **S1** as compared with **S2**. The relatively small **S1**, in comparison with **S2**, did not show substantial emission enhancement in the aggregated state, whereas the naphthyl group in **S2** was instrumental in restraining the non-radiative pathways with the enhancement of AIE. Moreover, the longer-wavelength emission of **S2** is possibly due to the extension of the aromatic ring system, resulting in greater electron delocalisation. By contrast to **S1** and **S2**, on increasing the water fraction, **S3** demonstrated ON/OFF/ON AIE behaviour, with a bathochromic shift in emission that corresponds to the near coplanar orientation of the naphthofuran rings in the axially chiral (*R*)-BINOL molecule. Although the luminogens **S3** and **S4** have structural similarities, the introduction of the dicyanovinylidene group into **S4** resulted in marked differences in their AIE behaviour. The introduction of the dicyanovinylidene unit generated sufficient steric hindrance to enhance the twist in the molecular conformation of **S4**. Therefore, the sterically induced enhanced non-coplanarity and twist in **S4** as compared with **S3** contributes to the enhanced TICT effect, which led to redshifted emission. With increasing water fraction, ACQ was predominant until $f_w = 50\%$; however, a steady enhancement of the emission intensity was observed with further increasing water fraction, which encumbered the rotation of the phenyl units and reduced the non-radiative transition, ultimately enhancing the PL intensity.

The fluorescence quantum yields (Φ) of **S1**--**S4** were subsequently measured in pure acetone as well as in acetone/H_2O, with $f_w = 90\%$ H_2O, by a comparison method, taking quinine sulfate as the standard ($\Phi = 0.54$ in 0.5 mL L^{-1} H_2SO_4). The quantum yields of **S1**--**S4** are presented in Table 2. The results demonstrate that the quantum yields of the fluorophores and the fluorescence efficiencies are directly correlated.

Table 2. Quantum yields of **S1**–**S4** in solution and the aggregated state.[a]

Compd	Solution state In pure acetone		Aggregated state In acetone/H_2O (10:90)	
	λ_{em} [nm]	Φ_{sol}[b] [%]	λ_{em} [nm]	Φ_{agg}[c] [%]
S1	410	0.084	467	0.028
S2	475.5	0.073	483.5	0.423
S3	489.5	5.817	496	6.229
S4	561	3.753	564	4.341

[a] Quinine sulfate in 0.1 M H_2SO_4 was used as standard ($\Phi = 0.54$). [b] Φ_{sol} = fluorescence quantum yield in solution. [c] Φ_{agg} = fluorescence quantum yield in the aggregated state.

Contrary to the low quantum yields (almost 0.2%)[48] observed for BINOL derivatives, the present strategy provides an effective method for designing fluorophores possessing large Stokes shifts that could effectively overcome imaging interference and therefore be used as bioprobes for cell imaging.

It is reasoned that the enhancement of emission intensity is induced by the formation of aggregates, which is confirmed by the SEM images of the non-aggregated **S3** and the aggregate of **S3** formed in 90% water/acetone, and by the observance of the Tyndall effect. The SEM images clearly distinguish the non-aggregated and aggregated forms of the fluorophore **S3**, supported by the observance of the Tyndall effect, an attribute of aggregate formation (Figure 9a–c). A similar Tyndall effect was also noticed when laser light was passed through aggregates of the other fluorophores **S1**, **S2** and **S4** (Figure 9d–g).

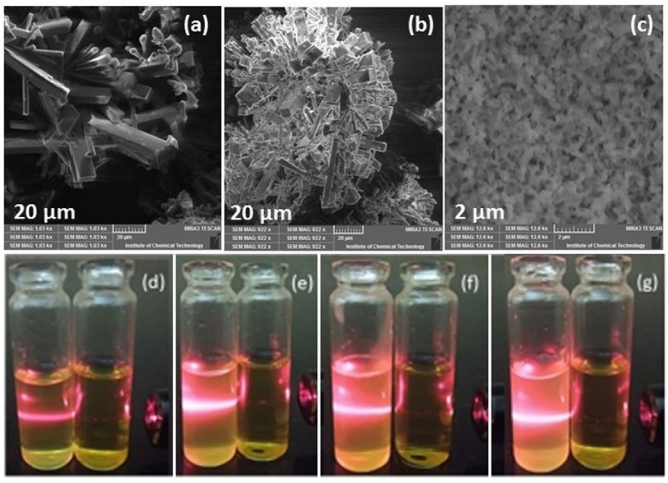

Figure 9. SEM images of (a) the non-aggregated state and (b,c) the aggregated state of **S3**. (d–g) Tyndall effect observed for (d) **S1**, (e) **S2**, (f) **S3** and (g) **S4** in their highest aggregated state (at $f_w = 40$, 90, 90 and 70% H_2O respectively).

Circular dichroism spectra of S3 and S4

Next, we explored whether the fused furans in the (*R*)-BINOL scaffold could bestow the AIEgens with chirality. Thus, we examined the circular dichroism spectra of the prepared AIEgens **S3** and **S4** to gain insights into their absolute configurations. The CD spectra of (*R*)-[9,9′-binaphtho[2,3-*b*]furan]-2,2′-diylbis(phenylmethanone) (**S3**) and (*R*)-2,2′-([9,9′-binaphtho[2,3-*b*]furan]-2,2′-diylbis(phenylmethylidene))dimalononitrile (**S4**) in acetone (concentration = 10^{-4} M) confirmed that after fusing the furan ring to (*R*)-BINOL, both **S3** and **S4** retained its chirality (Figure 10), with the absolute stereochemistry being transmitted from the (*R*)-BINOL to the AIEgens **S3** and **S4**.

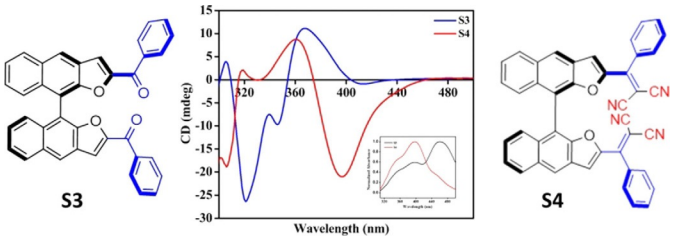

Figure 10. CD spectra of **S3** and **S4** in acetone. The inset shows the UV/Vis spectra of **S3** and **S4**.

The CD wavelength maxima obtained from the CD spectra of **S3** and **S4** at 411 and 397 nm, respectively, are more redshifted than that of (*R*)-BINOL (320 nm). The molar ellipticity ([θ]) values of **S3** and **S4** at 411 and 397 nm are 244010 and 5927880 mdeg mL mmol^{-1} mm^{-1}, respectively. These CD data indicate that the Knoevenagel condensation of **S3** with malononitrile affects the chirality more than the fusion of the furan ring to the (*R*)-BINOL skeleton. To evaluate the unique phenomenon of the aggregation-induced CD effect, we recorded the CD spectra of **S3** and **S4** in acetone/H_2O mixtures with different f_w (water fraction ranging from 0 to 99%).

Interestingly, the CD spectra of the AIEgens **S3** and **S4** were redshifted by about 21 and 10 nm, respectively, with increasing water fraction (f_w) from 0 to 99% in the acetone/H_2O mixture (Figure 11).

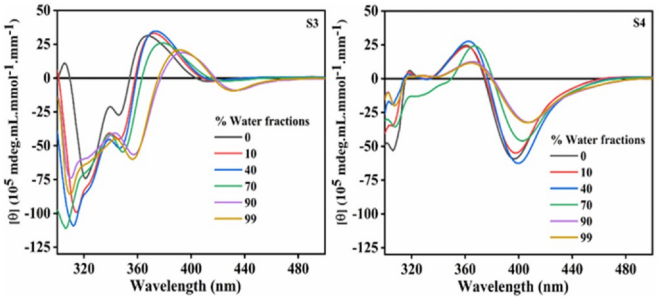

Figure 11. CD spectra of **S3** and **S4** in acetone/water mixtures with different f_w (concentration = 0.00355 g L^{-1}).

The AIEgen **S3** displayed enhancement of the CD signal with the addition of 10% H_2O, followed by a sharp annihilation of the CD signals, which continued until $f_w = 70\%$ H_2O. The addition of water beyond 70% resulted in a slight enhancement of the CD signal together with a redshift of the wavelength maximum, which thereafter remained constant until $f_w = 99\%$ H_2O. However, **S4** demonstrated a continuous enhancement of the

CD signals up to $f_w = 90\%$ H_2O addition, with a marginal fall of the CD signal observed at $f_w = 99\%$ H_2O addition. This CD annihilation and enhancement are represented by a graphical plot of the intensity of the circular dichroism signal versus f_w for **S3** and **S4** in Figure 12.

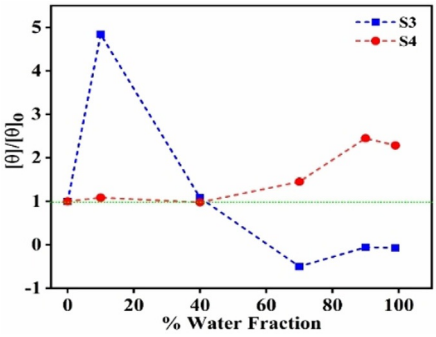

Figure 12. Plots of the relative molar ellipticity of **S3** (@346 nm) and **S4** (@396 nm) versus f_w. $[\theta]$ = molar ellipticity, $[\theta]_0$ = molar ellipticity at $f_w = 0\%$.

Interestingly, the luminogens **S3** and **S4** displayed dissimilar aggregation-induced CD signals. As already reported in the literature,[49,50] the reduction of the CD signal is generally a consequence of the decrease in the torsion angle between the adjacent naphthalene rings of (*R*)-BINOL. Therefore, it is reasoned that the corresponding torsion angle in **S3** has reduced in the aggregated state, observed beyond 40% water addition. However, the sharp spike observed in the CD spectrum with 10% water could be a result of conformational unlocking, causing a widening of the torsion angle, which then progressively lowers as the extent of aggregation is enhanced, causing a steep fall in the CD signal.

However, for **S4**, a non-bonding conformational locking arising from the incorporation of the dicyanovinylidene group causes severe steric hindrance, resulting in the enhancement of the torsion angle and an increase in the intensity of the CD signal.[49,50] The increase in the torsion angle due to severe steric strain is explained as follows: owing to the larger size of the -C=C(CN)$_2$ group in compound **S4**, as compared with -C=O in **S3**, the phenyl group at the β position with respect to -CN of the vinyl system is freer to adopt a coplanar disposition. Thus, the close proximity of the -CN groups to the phenyl ring allows a stronger interaction than is the case for -C=O in **S3**, thereby enhancing the torsion angle.[49,50] The overlay of the energy-minimised structures of the luminogens **S3** and **S4** shows a greater dihedral angle between the naphthyl rings of the (*R*)-BINOL in **S4** arising from steric hindrance (Figure 13). Thereby, a small structural modification can result in the inversion of aggregation-induced CD behaviour in the designed molecules, and this provides us with a handle to tune the chiroptical properties of the molecules. The variation in the torsion angle between the two naphthyl rings is responsible for the abnormal aggregation-annihilated CD (AACD), which impedes the observation of the CD phenomenon in the condensed state. Although a few attractive approaches have been reported in the literature to surpass the AACD effect in BINOL,

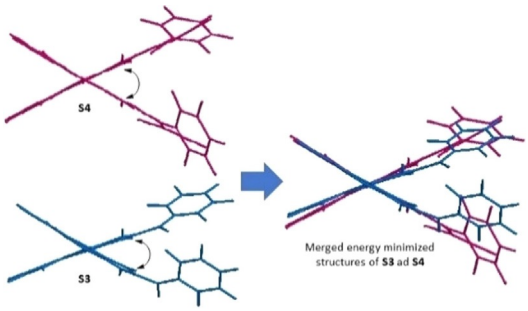

Figure 13. Energy-minimised structures of the luminogens **S3** and **S4.**

the precise control of circular dichroism in the aggregated state remains a formidable challenge.[51,52]

Cell imaging

The unique AIE properties exhibited by these chiral luminogens are attractive features that render them as potential fluorescent bioprobes for cell imaging. However, the problems of solubility and cell internalisation as well as the inherent ACQ of BINOL have limited the use of BINOL-based scaffolds for such applications. However, the high fluorescence quantum yield and large Stokes shift of **S4**, known not to show biological autofluorescence, provoked us to evaluate the efficacy of **S4** as a bioprobe for cell imaging. Although AIEgens are potentially useful agents for bioimaging, they must be biocompatible for any potential biological application. Hence, the in vitro biocompatibility of **S4** was evaluated in mouse fibroblast cells L929.[49] The details of the experimental procedures are provided in the Supporting Information. Resorufin, a blue-coloured non-fluorescent dye, was used to quantify the percentage cell viability and it was found that **S4** is highly biocompatible with these cells at concentrations in the range 10–100 $\mu g\,mL^{-1}$ (with ca. 100% viability; Figure 14; negative control: cells + media only; positive control: cells + Triton-X + media; Triton-X: non-ionic surfactant that is used for cell lysis).[53–55]

After the confirmation of cellular uptake, a cellular localisation study was carried out on L929 cells by using confocal laser imaging to determine the extent of internalisation in the

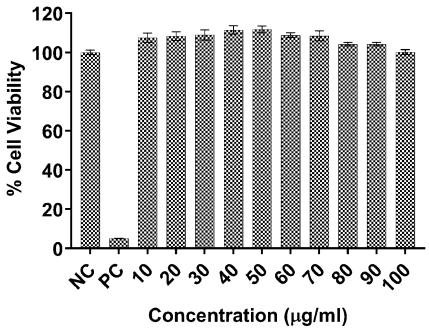

Figure 14. Histogram showing the viability of L929 cells with compound **S4** at concentrations ranging from 10 to 100 $\mu g\,mL^{-1}$. NC = negative control, PC = positive control.

cell and the effect on cell morphology.[56] The cellular uptake of **S4** in MD-MB-231 cancer cells was analysed by seeding the cancer cells on sterile coverslips in 12-well plates (50 000 cells per well) and incubating for 24 h. Next, 25 μg mL^{-1} **S4** was added to the well plates and incubation performed for a further 24 h. The excess material in the cells was washed gently with phosphate-buffered saline (PBS), and then 4% paraformaldehyde was used to fix the cells for 15 min, followed by washing with PBS. 4′,6-Diamidino-2-phenylindole (DAPI; 2 μg mL^{-1}) was used for nuclear staining over a period of 5 min. The cells were then mounted on a glass slide, sealed, and analysed by confocal laser scanning microscopy (Leica SP8, Leica Microsystems).[57,58]

DAPI stains the nuclei blue, and the appearance of green fluorescence in the aggregate state can be explained by membrane protein interactions, which restrict intramolecular rotation as well as the non-radiative decay of the excitons, resulting in an enhancement of fluorescence intensity (Figure 15). The interactions could be the result of strong hydrogen bonding between the cyano groups of **S4** and the peptide bonds present in the cells.

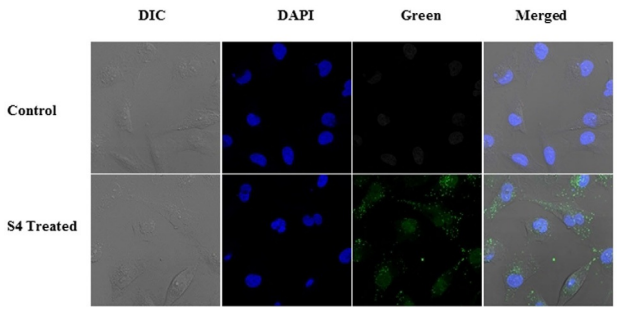

Figure 15. Cellular internalisation of **S4** in MDA-MB-231 cells. DIC = Differential interference contrast imaging, used to visualize unstained or transparent samples

The overlay of the bright field and fluorescence images confirmed that the **S4** taken up by the cells is uniformly dispersed in the cytoplasm and not co-localised within the nuclei. No green signals were observed in the control cells and all the cells retained their morphology. The mean fluorescence intensity was calculated, and the results are shown in the histogram in Figure 16. This investigation revealed that **S4** selectively labels the cytoplasm over the nucleus with a high mean fluorescence intensity as well as possesses excellent biocompatibility over a wide range of concentrations and could therefore be used as an excellent imaging agent in living cells.

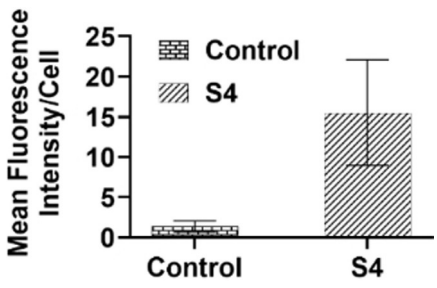

Figure 16. Histogram depicting the mean fluorescence intensity per cell of **S4** in comparison with the control.

Conclusions

We have demonstrated the successful design and synthesis of a new series of luminogens by fusing a 2-phenacylfuran component to aromatic units possessing solid-state emitting properties. The systematic study of their photophysical, electrochemical, thermal and AIE properties, as well as their single-crystal packing structures, revealed that the fusion of 2-phenacylfuran derivatives to the aromatic core of BINOL generated an overall distorted geometry that is instrumental in reducing intermolecular π–π stacking through the presence of large sterically hindering groups, thereby endowing the fluorophores with enhanced emissive properties in the aggregated state. The CD spectra further confirmed the chirality transfer from BINOL that renders both the luminogens **S3** and **S4** chiral. Both chiral luminogens demonstrated excellent solid-state emissive properties, possessing high thermal stability and the opportunity for wavelength tunability. Compared with typical BINOL derivatives, AIEgens **S2**–**S4** exhibit large Stokes shifts and high fluorescence quantum yields. In addition to its high fluorescence quantum yield and large Stokes shift, **S4** also demonstrates excellent biocompatibility over the concentration range 10–100 μg mL^{-1}. Therefore, the efficacy of **S4** as a fluorescent bioprobe for cell imaging was explored. It was observed that **S4** was well internalised and uniformly dispersed within the cytoplasm in MDA-MB-231 cancer cells, showing high fluorescence intensity. Altogether, the design strategies demonstrated here could pave the way to the development of next-generation chiral fluorescent probes for diverse applications.

Experimental Section

Chemicals and reagents: Salicylaldehyde (**1a**), 2-bromoacetophenone (**2**), 2-hydroxynaphthaldehyde (**1b**) and (*R*)-BINOL (**5**) were purchased from Sigma–Aldrich. Malononitrile, *n*BuLi, piperidine, pyridine, *N*,*N*,*N*′,*N*′-tetramethylethylenediamine (TMEDA) and BBr_3 were purchased from Spectrochem. Ultrapure water (> 18 MΩ cm) from a Milli-Q reference system (Millipore) was employed throughout.

General experimental procedures, analysis and instrumental details are provided in the Supporting Information.

Procedures and characterisation: Compounds **3**, **4** and **6**–**8** have been previously reported in the literature and were synthesised following the reported protocols. The spectral data were in agreement with the literature values.[59–63]

Synthesis of benzofuran-2-yl(phenyl)methanone (3):[51] A mixture of 2-hydroxybenzaldehyde (**1a**; 0.290 g, 2.374 mmol) and 2-bromo-1-phenylethanone (**2**; 0.519 g, 2.611 mmol) were dissolved in acetone, K_2CO_3 (0.984 g, 7.122 mmol) was added, and the mixture was heated to reflux under continuous stirring for 12 h. After consumption of compound **1a** (as monitored by TLC), the reaction mixture was quenched by the addition of water and the organic layer was

extracted with ethyl acetate (3×10 mL). The combined organic layers were dried over anhydrous sodium sulfate, filtered and evaporated to dryness. The residue was purified by column chromatography over silica gel (cyclohexane/ethyl acetate, 90:10) to afford the desired product **3** (0.503 g, 2.256 mmol, 95%) as a white powder ^{1}H NMR (300 MHz, $CDCl_3$): $\delta = 8.06$ (d, $J = 8.1$ Hz, 2H), 7.70 (d, $J = 7.9$ Hz, 1H), 7.61 (t, $J = 8.1$ Hz, 2H), 7.53 (s, 1H),7.54–7.45 (m, 3H), 7.29 ppm (dd, $J = 7.3$, 15.1 Hz, 1H); ^{13}C NMR (75 MHz, $CDCl_3$): $\delta = 184.4$, 155.7, 152.2, 137.1, 132.8, 128.7, 128.2, 127.0, 124.0, 123.3, 116.5, 112.5 ppm; IR (neat): $\tilde{\nu} = 3140$, 3056, 1641, 1543, 1329, 1215, 970, 744, 692 cm^{-1}.

Synthesis of 2-[benzofuran-2-yl(phenyl)methylene]malononitrile (S1): Compound **3** (0.500 g, 2.231 mmol) and malononitrile (0.442 g, 6.695 mmol) were added dropwise to pyridine (10 mL) in a round-bottomed flask maintained at 0 °C. After complete addition, the mixture was stirred for 10 min and then heated at reflux overnight. After the consumption of starting material **3** (monitored by TLC), the reaction mixture was quenched with water and extracted with DCM. The organic layer was collected, dried over anhydrous Na_2SO_4 and evaporated to dryness. The crude product was subjected to column chromatography using ethyl acetate/petroleum ether (1:9) as eluent to afford compound **S1** (0.444 g, 1.64 mmol, 73%) as a yellow solid. M.p. 177–181 °C; ^{1}H NMR (400 MHz, $CDCl_3$): $\delta = 7.62$ (t, $J = 8.9$ Hz, 3H), 7.53 (dt, $J = 10.9$, 7.8 Hz, 5H), 7.31 (t, $J = 7.5$ Hz, 1H), 7.04 ppm (s, 1H); ^{13}C NMR (126 MHz, $CDCl_3$): $\delta = 157.8$, 156.8, 150.7, 133.1, 131.8, 129.7, 129.5, 129.0, 127.3, 124.5, 123.0, 120.5, 113.8, 113.4, 112.5, 79.4 ppm; HRMS (ESI): *m/z* calcd for $C_{18}H_{10}N_2O$: 270.0793 $[M]^+$; found: 270.0810.

Synthesis of naphtho[2,1-*b*]furan-2-yl(phenyl)methanone (4):[52] A mixture of 2-hydroxy-1-naphthaldehyde (**1b**; 0.335 g, 1.945 mmol) and 2-bromo-1-phenylethanone (**2**; 0.425 g, 2.14 mmol) were dissolved in acetone, K_2CO_3 (0.806 g, 8.84 mmol) was added and the reaction mixture heated at reflux for 12 h. After consumption of the starting material **1b** (as monitored by TLC), the reaction was quenched with water and the organic layer was extracted with ethyl acetate (3×10 mL). The combined organic layers were dried over anhydrous sodium sulfate, filtered and evaporated to dryness. The residue was purified by column chromatography over silica gel (cyclohexane/ethyl acetate, 95:5) to afford the desired product **4** (0.493 g, 1.810 mmol, 93%) as a brown powder. ^{1}H NMR (300 MHz, $CDCl_3$): $\delta = 8.00$ (d, $J = 8.1$ Hz, 1H), 7.94–7.98 (m, 2H), 7.92 (dd, $J = 9.0$, 4.1 Hz, 1H), 7.59–7.72 (m, 7H), 7.56 ppm (d, $J = 4.3$ Hz, 1H); ^{13}C NMR (75 MHz, $CDCl_3$): $\delta =$ 182.1, 162.0, 155.2, 138.3, 132.6, 130.1, 130.0, 129.9, 128.9, 128.8, 128.3, 127.1, 127.3, 127.2, 125.0, 124.0, 121.6, 116.6, 111.3 ppm; IR (neat): $\tilde{\nu} = 3130$, 3045, 1668, 1545 cm^{-1}.

Synthesis of 2-[naphtho[2,1-*b*]furan-2-yl(phenyl)methylene]malononitrile (S2): Pyridine (10 mL) was added dropwise to a mixture of naphtho[2,1-*b*]furan-2-yl(phenyl)methanone (**4**; 0.457 g, 1.681 mmol) and malononitrile (0.442 g, 6.695 mmol) in a round-bottomed flask, maintained at 0 °C. The mixture was stirred for 10 min and then heated at reflux overnight. After the consumption of starting material **4** (monitored by TLC), the reaction was quenched by water and extracted with DCM. The collected organic layer was dried over anhydrous Na_2SO_4, filtered and evaporated to dryness. The crude product was subjected to column chromatography using ethyl acetate/petroleum ether (1:9) as eluent to afford compound **S2** (0.399 g, 1.24 mmol, 68%) as a yellow solid. M.p. 157–164 °C; ^{1}H NMR (400 MHz, $CDCl_3$): $\delta = 8.03$ (d, $J = 7.4$ Hz, 1H), 7.93–7.96 (m, 2H), 7.72 (dd, $J_1 = 4.1$ Hz, $J_2 = 9.0$, 1H), 7.53–7.65 (m, 7H), 7.48 ppm (d, $J = 4.3$ Hz, 1H); ^{13}C NMR (126 MHz, $CDCl_3$): $\delta =$ 157.1, 155.9, 150.2, 133.3, 131.8, 130.6, 129.5, 129.3, 129.0, 128.0, 127.4, 126.2, 123.8, 123.4, 119.3, 114.1, 113.8, 112.5, 77.8 ppm; HRMS (ESI): *m/z* calcd for $C_{22}H_{12}N_2O$: 320.0949 $[M]^+$; found: 320.0940.

Synthesis of (*R*)-2,2′-dimethoxy-1,1′-binaphthalene (6):[49] K_2CO_3 (4.855 g, 35.131 mmol) and methyl iodide (2.43 mL, 39.035 mmol) were added to a solution of (*R*)-BINOL (**5**; 2.235 g, 7.807 mmol) in acetone (50 mL), and the mixture was then stirred while heating at reflux for 12 h. The mixture was then cooled to room temperature and water (40 mL) was added. The resulting suspension was stirred for 4 h at room temperature and filtered. The resulting white solid was washed with water and dried to give the desired product **6** (2.43 g, 7.73 mmol, 99%) as a white solid. ^{1}H NMR (300 MHz, $CDCl_3$): $\delta = 3.77$ (s, 6H), 7.08–7.36 (m, 6H), 7.46 (d, 2H, $J = 9.3$ Hz), 7.87 (d, 2H, $J = 7.3$ Hz), 7.98 ppm (d, 2H, $J = 8.8$ Hz); ^{13}C NMR (75 MHz, $CDCl_3$): $\delta = 57.0$, 114.7, 120.1, 123.9, 125.7, 126.7, 128.3, 129.6, 129.8, 134.4, 155.4 ppm; IR (neat): $\tilde{\nu} = 3065$, 3010, 2954, 2934, 2837, 1618, 1590, 1505, 1460 cm^{-1}.

Synthesis of (*R*)-2,2′-dimethoxy-[1,1′-binaphthalene]-3,3′-dicarbaldehyde (7):[50] TMEDA (2.40 mL, 16.41 mmol) was addded portionwise to a suspension of **6** (2.0 g, 6.56 mmol) in dry diethyl ether (40 mL) under N_2 at room temperature. After cooling the mixture to 0 °C, a 2.5 M solution of *n*-butyllithium in hexanes (10.2 mL, 29.02 mmol) was added dropwise and the mixture stirred at 0 °C for 1 h before warming up to ambient temperature and heating at reflux overnight. The resulting yellow-brown suspension was cooled to −78 °C, anhydrous DMF (4.0 mL, 52.5 mmol) was added dropwise and the white suspension stirred at room temperature for 2 h. Next, 2 N aq. HCl (40 mL) was added and the mixture stirred for 30 min. The aqueous and organic phases were separated and the organic layer was washed successively with 1 M HCl (20 mL), saturated aqueous sodium bicarbonate (20 mL) and brine (20 mL) before finally drying with anhydrous Na_2SO_4. The solvent was evaporated and the resulting sticky yellow mass was purified by silica gel column chromatography (EtOAc/hexane, 3:7) to give **7** (2.14 g, 5.78 mmol; 88%) as a pale-yellow solid. ^{1}H NMR ($CDCl_3$, 400 MHz): $\delta = 3.42$ (s, 6H), 7.17 (d, $J = 8.4$ Hz, 2H), 7.46 (t, $J = 6.6$ Hz, 2H), 7.56 (t, $J = 6.4$ Hz, 2H), 8.09 (d, $J = 8.8$ Hz, 2H), 8.97 (s, 2H), 10.56 ppm (s, 2H); IR (KBr): $\tilde{\nu} = 1678$, 1460, 1390, 1254 cm^{-1}; MS: *m/z*: 370.12 $[M]^+$.

Synthesis of (*R*)-2,2′-dihydroxy-[1,1′-binaphthalene]-3,3′-dicarbaldehyde (8):[51] Compound **7** (2.318 g, 6.259 mmol) was dissolved in DCM (30 mL) in an oven-dried two-necked flask. BBr_3 (1.8 mL, 18.78 mmol) in DCM (10 mL) was then added dropwise at 0 °C. The mixture was stirred for 12 h at room temperature and then water (20 mL) was added dropwise. After stirring at room temperature for 2 h, the aqueous layer was extracted with DCM (3×30 mL) and the combined organic layers were dried over Na_2SO_4, filtered and evaporated. Purification over silica with ethyl acetate as eluent furnished product **8** (2.1 g, 6.134 mmol, 98%) as a yellow solid. ^{1}H NMR (300 MHz, $CDCl_3$): $\delta = 7.11$–7.15 (m, 2H), 7.32–7.36 (m, 4H), 7.93–7.97 (m, 2H). 8.32 (s, 2H), 9.13 (s, 2H), 10.53 ppm (s, 2H); elemental analysis calcd (%) for $C_{14}H_{10}O_4$: C 69.42, H 4.16; found: C 69.40, H 4.10

Synthesis of (*R*)-[9,9′-binaphtho[2,3-*b*]furan]-2,2′-diylbis(phenylmethanone) (S3): K_2CO_3 (6.136 g, 44.40 mmol) was added to a solution of compound **8** (1.9 g, 5.55 mmol) and 1-phenyl-2-bromoethanone (2.66 g, 13.32 mmol) in acetone under N_2. The resulting mixture was heated at reflux with stirring overnight. After removal of the solvent, water and ethyl acetate were added. The aqueous layer was extracted three times with ethyl acetate. The combined organic layers were washed with brine, dried over $MgSO_4$, filtered and concentrated under reduced pressure. The residue was purified by column chromatography over silica gel with ethyl acetate/

petroleum ether (1:9) as eluent to afford **S3** (2.46 g, 4.54 mmol, 82%) as a yellow solid. M.p. 240–242 °C; ^{1}H NMR (400 MHz, $CDCl_3$): δ = 8.45 (s, 2H), 8.13 (d, J = 8.3 Hz, 2H), 7.87–7.82 (m, 6H), 7.55–7.49 (m, 4H), 7.45 (t, J = 7.4 Hz, 2H), 7.39–7.35 (m, 2H), 7.24 ppm (t, J = 7.6 Hz, 4H); ^{13}C NMR (126 MHz, $CDCl_3$): δ = 112.9, 12.3, 124.6, 126.0, 126.6, 127.4, 128.2, 129.1, 129.7, 131.3, 132.5, 132.9, 136.5, 152.8, 154.58, 183.9 ppm; HRMS (ESI): m/z calcd for $C_{38}H_{22}O_4$: 542.1518 $[M+H]^+$; found: 543.1572.

Synthesis of (*R*)-2,2′-([9,9′-binaphtho[2,3-b]furan]-2,2′-diylbis(phenylmethanylylidene))dimalononitrile (S4): Compound **S3** (0.200 g, 0.3686 mmol) and malononitrile (0.073 g, 1.10 mmol) were added dropwise at 0 °C to pyridine (10 mL) in a round-bottomed flask in an ice bath. After stirring for 10 min, the mixture was heated at reflux overnight. After consumption of **S3** (as monitored by TLC), the reaction was quenched by the addition of water and the mixture extracted with DCM. The collected organic layer was dried over anhydrous Na_2SO_4 and evaporated to dryness. The residue was subjected to column chromatography using ethyl acetate/petroleum ether (1:9) as eluent to afford **S4** (0.141 g, 0.22 mmol, 60%) as a red solid. M.p. 214–216 °C; ^{1}H NMR (400 MHz, $CDCl_3$): δ = 7.10 (s, 2H), 7.36 (t, J = 8.0 Hz, 2H), 7.61–7.45 (m, 14H), 8.09 (d, J = 8.2 Hz, 2H), 8.33 ppm (s, 2H); ^{13}C NMR (126 MHz, $CDCl_3$): δ = 80.4, 112.1, 112.8, 113.9, 120.7, 123.4, 124.8, 125.9, 127.3, 127.8, 128.9, 129.6, 131.2, 131.7, 132.9, 133.2, 153.6, 153.7, 157.3 ppm; HRMS (ESI): m/z calcd for $C_{44}H_{22}N_4O_2$: 638.1742 $[M+H]^+$; found: 639.1756.

Crystallographic data: Deposition numbers 1984512 (**S1**), 1984513 (**S2**), and 1984516 (**S3**) contain the supplementary crystallographic data for this paper. These data are provided free of charge by the joint Cambridge Crystallographic Data Centre and Fachinformationszentrum Karlsruhe Access Structures service.

Acknowledgements

V.P.J. is thankful to the CSIR for a Senior Research Fellowship. G.Y. is thankful to the CoE-PI (TEQIP-III) and a Sarthi Fellowship. P.K. acknowledges TEQIP-III for providing the opportunity to work at ICT as a summer intern. The authors also acknowledge SAIF-IIT Mumbai for the HRMS analysis and CIF, SPPU for single-crystal X-ray diffraction analysis. S.S. acknowledges DST-SERB, CSIR, UGC-Start-Up grant, as well as TEQIP-III CoE-PI for the financial assistance.

Conflict of interest

The authors declare no conflict of interest.

Keywords: aggregation · biaryls · chirality · imaging agents · luminescence

[1] C. H. J. Queisser, *J. Lumin.* **1981**, *24*, 3–10.
[2] M. Huang, R. Yu, K. Xu, S. Ye, S. Kuang, X. Zhu, Y. Wan, *Chem. Sci.* **2016**, *7*, 4485–4491.
[3] S. Jhulki, J. N. Moorthy, *J. Mater. Chem. C* **2018**, *6*, 8280–8325.
[4] O. Ostroverkhova, *Chem. Rev.* **2016**, *116*, 13279–13412.
[5] P. Yu, Y. Zhen, H. Dong, W. Hu, *Chem* **2019**, *5*, 2814–2853.
[6] Y. Yin, M. U. Ali, W. Xie, H. Yang, H. Meng, *Mater. Chem. Front.* **2019**, *3*, 970–1031.
[7] H. Sasabe, J. Kido, *Chem. Mater.* **2011**, *23*, 621–630.
[8] D. Cao, Z. Liu, P. Verwilst, S. Koo, P. Jangjili, J. S. Kim, W. Lin, *Chem. Rev.* **2019**, *119*, 10403–10519.
[9] K. Zhang, J. Liu, Y. Zhang, J. Fan, C. K. Wang, L. Lin, *J. Phys. Chem. C* **2019**, *123*, 24705–24713.
[10] U. P. Pandey, P. Thilagar, *Adv. Optical Mater.* **2020**, *8*, 1902145.
[11] J. Li, J. Wang, H. Li, N. Song, D. Wang, B. Z. Tang, *Chem. Soc. Rev.* **2020**, *49*, 1144–1172.
[12] T. Usuki, M. Shimada, Y. Yamanoi, T. Ohto, H. Tada, H. Kasai, E. Nishibori, H. Nishihara, *ACS Appl. Mater. Interfaces* **2018**, *10*, 12164–12172.
[13] M. Gao, Y. Li, X. Chen, S. Li, L. Ren, B. Z. Tang, *ACS Appl. Mater. Interfaces* **2018**, *10*, 14410–14417.
[14] X. Wang, P. Song, L. Peng, A. Tong, Y. Xiang, *ACS Appl. Mater. Interfaces* **2016**, *8*, 609–616.
[15] P. Gopikrishna, N. Meher, P. K. Iyer, *ACS Appl. Mater. Interfaces* **2018**, *10*, 12081–12111.
[16] J. Mei, N. L. C. Leung, R. T. K. Kwok, J. W. Y. Lam, B. Z. Tang, *Chem. Rev.* **2015**, *115*, 11718–11940.
[17] Z. Jiang, T. Gao, H. Liu, M. S. S. Shaibani, Z. Liu, *Dyes Pigments* **2020**, *175*, 108168–108176.
[18] H. Zhang, X. Zheng, R. T. K. Kwok, J. Wang, N. L. C. Leung, L. Shi, J. Z. Sun, Z. Tang, J. W. Y. Lam, A. Qin, B. Z. Tang, *Nat. Commun.* **2018**, *9*, 4961.
[19] S. Chen, W. Liu, Z. Ge, W. Zhang, K. Wang, Z. Hu, *Spectrochim. Acta Part A* **2018**, *193*, 141–146.
[20] H. Yang, K. Xiang, Y. Li, S. Li, C. Xu, *J. Organomet. Chem.* **2016**, *801*, 96–100.
[21] T. Kinuta, N. Tajima, M. Fujiki, M. Miyazawa, Y. Imai, *Tetrahedron*, **2012**, *68*, 4791–4796.
[22] F. Song, Z. Xu, Q. Zhang, Z. Zhao, H. Zhang, W. Zhao, Z. Qiu, C. Qi, H. Zhang, H. H. Y. Sung, I. D. Williams, J. W. Y. Lam, Z. Zhao, A. Qin, D. Ma, B. Z. Tang, *Adv. Funct. Mater.* **2018**, *28*, 1800051–1800063.
[23] J. C. Y. Ng, J. Liu, H. Su, Y. Hong, H. Li, J. W. Y. Lam, K. S. Wong, B. Z. Tang, *J. Mater. Chem. C* **2014**, *2*, 78–83.
[24] N. Li, H. Feng, Q. Gong, C. Wu, H. Zhou, Z. Huang, J. Yang, X. Chen, N. Zhao, *J. Mater. Chem. C* **2015**, *3*, 11458–11463.
[25] Y. Wang, Y. Zhang, W. Hu, Y. Quan, Y. Li, Y. Cheng, *ACS Appl. Mater. Interfaces* **2019**, *11*, 26165–26173.
[26] M. Hu, H.-T. Feng, Y.-X. Yuan, Y.-S. Zheng, B. Z. Tang, *Coord. Chem. Rev.* **2020**, *416*, 213329–223351.
[27] G. Albano, F. Salerno, L. Portus, W. Porzio, L. A. Aronica, L. D. Bari, *ChemNanoMat* **2018**, *4*, 1059–1070.
[28] G. Albano, M. Lissia, G. Pescitelli, L. A. Aronica, L. D. Bari, *Mater. Chem. Front.* **2017**, *1*, 2047–2056.
[29] S. Saha, C. Schneider, *Chem. Eur. J.* **2015**, *21*, 2348–2352.
[30] S. Saha, S. K. Alamsetti, C. Schneider, *Chem. Commun.* **2015**, *51*, 1461–1464.
[31] S. Saha, C. Schneider, *Org. Lett.* **2015**, *17*, 648–652.
[32] L. Pu, *Acc. Chem. Res.* **2012**, *45*, 150–163.
[33] D. Parmar, E. Sugiono, S. Raja, M. Rueping, *Chem. Rev.* **2014**, *114*, 9047–9153.
[34] H. T. Feng, C. Liu, Q. Li, H. Zhang, J. W. Y. Lam, B. Z. Tang, *ACS Mater. Lett.* **2019**, *1*, 192–202.
[35] Z. Jiang, J. Wang, T. Gao, J. Ma, R. Chen, Z. Liu, *ACS Appl. Mater. Interfaces* **2020**, *12*, 9520–9527.
[36] C. Liu, G. Yang, Y. Si, X. Pan, *J. Phys. Chem. C* **2018**, *122*, 5032–5039.
[37] V. P. Jejurkar, G. Yashwantrao, B. P. K. Reddy, A. P. Ware, S. S. Pingale, R. Srivastava, S. Saha, *ChemPhotoChem* **2020**, *4*, 691–703.
[38] F. Song, Z. Zhao, Z. Liu, J. W. Y. Lam, B. Z. Tang, *J. Mater. Chem. C* **2020**, *8*, 3284–3301.
[39] L. Shi, K. Li, P.-C. Cui, L.-L. Li, S.-L. Pan, M.-Y. Li, X.-Q. Yu, *J. Mater. Chem. B* **2018**, *6*, 4413–4418.
[40] A. S. Klymchenko, T. Ozturk, V. G. Pivovarenko, A. P. Demchenko, *Can. J. Chem.* **2001**, *79*, 358–363.
[41] A. M. Piloto, A. S. C. Fonseca, S. P. G. Costa, M. S. T. Goncalves, *Tetrahedron* **2006**, *62*, 9258–9267.
[42] W. A. Muriel, R. Morales-Cueto, W. Rodríguez-Córdoba, *Phys. Chem. Chem. Phys.* **2019**, *21*, 915–928.
[43] Gaussian 09, Revision D.01, M. J. Frisch, G. W. Trucks, H. B. Schlegel, G. E. Scuseria, M. A. Robb, J. R. Cheeseman, G. Scalmani, V. Barone, B. Mennucci, G. A. Petersson, H. Nakatsuji, M. Caricato, X. Li, H. P. Hratchian, A. F. Izmaylov, J. Bloino, G. Zheng, J. L. Sonnenberg, M. Hada, M. Ehara,

K. Toyota, R. Fukuda, J. Hasegawa, M. Ishida, T. Nakajima, Y. Honda, O. Kitao, H. Nakai, T. Vreven, Jr., J. A. Montgomery, J. E. Peralta, F. Ogliaro, M. Bearpark, J. J. Heyd, E. Brothers, K. N. Kudin, V. N. Staroverov, R. Kobayashi, J. Normand, K. Raghavachari, A. Rendell, J. C. Burant, S. S. Iyengar, J. Tomasi, M. Cossi, N. Rega, J. M. Millam, M. Klene, J. E. Knox, J. B. Cross, V. Bakken, C. Adamo, J. Jaramillo, R. Gomperts, R. E. Stratmann, O. Yazyev, A. J. Austin, R. Cammi, C. Pomelli, J. W. Ochterski, R. L. Martin, K. Morokuma, V. G. Zakrzewski, G. A. Voth, P. Salvador, J. J. Dannenberg, S. Dapprich, A. D. Daniels, O. Farkas, J. B. Foresman, J. V. Ortiz, J. Cioslowski, D. J. Fox, Gaussian Inc., Wallingford CT **2013**.

[44] The DFT calculations were repeated three times and no notable changes in the results were observed. The calculations were also carried out at three different levels, that is, B3LYP, M062X and BMK using the 6-311G + (d,p) basis set (gas phase).

[45] J. N. Zhang, H. Kang, N. Li, S. M. Zhou, H. M. Sun, S. W. Yin, N. Zhao, B. Z. Tang, *Chem. Sci.* **2017**, *8*, 577 – 582.

[46] *Solvent and Environmental Effects in Principles of Fluorescence Spectroscopy* (Ed.: J. R. Lakowicz), Springer, Boston, **2006**.

[47] H. S. Silva, A. Alfarra, G. Vallverdu, D. Bégué, B. Bouyssiere, I. Baraille, *Petroleum Sci.* **2019**, *16*, 669 – 684.

[48] Y. Wang, L. Hu, F. Zhao, S. Yu, J. Tian, D. Shi, X. Wang, X.-Q. Yu, L. Pu, *Chem. Eur. J.* **2017**, *23*, 17678.

[49] N. Zhao, W. Gao, M. Zhang, J. Yang, X. Zheng, Y. Li, R. Cui, W. Yin, N. Li, *Mater. Chem. Front.* **2019**, *3*, 1613 – 1618.

[50] C. Coluccini, P. T. Anusha, H-Y. T. Chen, S.-L. Liao, Y. K. Ko, A. Yabushita, C. W. Luo, Y. M. Ng, Y. L. Khung, *Sci. Rep.* **2019**, *9*, 12762.

[51] H. K. Zhang, H. K. Li, J. Wang, J. Z. Sun, A. J. Qin, B. Z. Tang, *J. Mater. Chem. C* **2015**, *3*, 5162 – 5166.

[52] H. K. Zhang, X. Zheng, R. T. K. Kwok, J. Wang, N. L. C. Leung, L. Shi, J. Z. Sun, Z. Y. Tang, J. W. Y. Lam, A. J. Qin, B. Z. Tang, *Nat. Commun.* **2018**, *9*, 4961.

[53] We assume that the viability could have varied as a result of the hormesis effect, in addition to any systemic errors. The viability exceeded 100% in Figure 14, which is within the acceptable range of 10% contributed to by the above-mentioned factors. For a more detailed view of Figure 14, please refer to biocompatibility.tiff file in the Supporting Information.

[54] P. Larsson, H. Engqvist, J. Biermann, E. W. Rönnerman, E. F. Aronsson, A. Kovács, P. Karlsson, K. Helou, T. Z. Parris, *Sci. Rep.* **2020**, *10*, 5798 – 5810.

[55] M. P. Mattson, *Ageing Res. Rev.* **2008**, *7*, 1 – 7.

[56] D. S. Chauhan, B. P. Reddy, S. K. Mishra, R. Prasad, M. Dhanka, M. Vats, G. Ravichandran, D. Poojari, O. Mhatre, A. De, R. Srivastava, *Langmuir* **2019**, *35*, 7805 – 7815.

[57] M. K. Kumawat, M. Thakur, R. B. Gurung, R. Srivastava, *ACS Sustainable Chem. Eng.* **2017**, *5*, 1382 – 1391.

[58] The excitation wavelength was 405 nm, and the emission wavelength range was 500–550 nm.

[59] A. Carrer, D. Brinet, P. Florent, E. Bertounesque, *J. Org. Chem.* **2012**, *77*, 1316 – 1327.

[60] M. L. N. Rao, D. K. Awasthi, D. Banerjee, *Tetrahedron Lett.* **2007**, *48*, 431 – 434.

[61] A. S. Castanet, F. Colobert, P.-E. Broutin, M. Obringer, *Tetrahedron: Asymmetry* **2002**, *13*, 659 – 665.

[62] Q. Li, H. Guo, Y. Wu, X. Zhang, Y. Liu, J. Zhao, *J. Fluoresc.* **2011**, *21*, 2077 – 2084.

[63] Y. N. Belokon, C. Denis, D. A. Borkin, L. V. Yashkina, A. V. Demitriev, D. Katayev, K. Michael, *Tetrahedron: Asymmetry* **2006**, *17*, 2328 – 2333.

Manuscript received: November 13, 2020
Accepted manuscript online: December 23, 2020
Version of record online: February 25, 2021